ACS APPLIED ELECTRONIC MATERIALS

pubs.acs.org/acsaelm

Article

Bioplausible Synaptic Behavior of Al/$Gd_{0.3}Ca_{0.7}MnO_3$/Au Memristive Devices for Unsupervised Spiking Neural Networks

Teemu Hynnä, Alejandro Schulman,* Ville Lähteenlahti, Hannu Huhtinen, and Petriina Paturi

Cite This: *ACS Appl. Electron. Mater.* 2024, 6, 292−298

Read Online

ACCESS | Metrics & More | Article Recommendations

ABSTRACT: Inspired by the biological nervous system, unsupervised spiking neural networks (SNNs) with the spike-timing-dependent plasticity (STDP) learning rule have been considered as the next-generation artificial neural networks (ANNs). However, to construct a functional SNN with high pattern recognition accuracy and low power consumption, hardware elements that present synaptic behavior still need to be developed. In this work, we studied $Gd_{0.3}Ca_{0.7}MnO_3$ (GCMO)-based memristive devices comprised of an asymmetrical electrode configuration, Al/GCMO/Au. We verified its switching properties, focusing on single pulse switching and its usability as artificial synapse by means of the STDP learning rule. The dynamic range is well controlled by the pulse amplitude and width, and the conductance change shows a clear dependence on the interval between the pulses. Moreover, pattern recognition accuracy (>87%) is obtained in biologically plausible unsupervised SNN simulations when the device characteristics are utilized as the synaptic weight in the network. The results shed some light on the complexity of the operation of the devices for utilization in unsupervised SNNs, that is, the evolution of the ANNs for which the first proof-of-concept is currently being reported. Additionally, the bioplausibility of the simulated network opens the door to considering biohybrid systems and their enormous application possibilities.

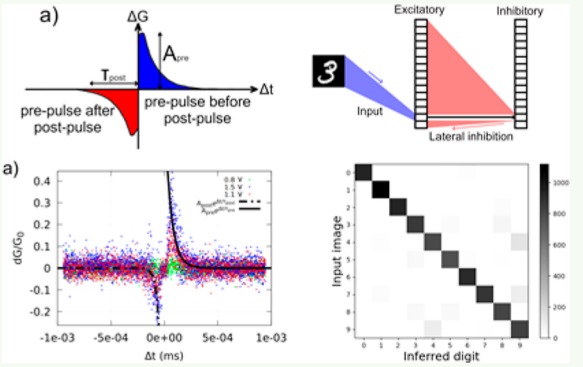

KEYWORDS: *memristors, perovskite oxides, thin films, neuromorphic computing, spiking neural networks*

INTRODUCTION

The development of neuromorphic computing systems has garnered significant attention due to their potential to mimic the intricate functionalities of the human brain.[1] One crucial aspect of such systems is the emulation of synapses, the pivotal connectors responsible for information transfer and storage in biological neural networks. The emergence of memristive materials has brought forth a promising avenue for the realization of artificial synapses,[2] enabling the construction of hardware-based brain-inspired computing architectures.

Moreover, a significant stride toward advancing the functionality of artificial synapses has been the integration into unsupervised spiking neural networks (SNNs). While real neurons communicate using spikes of potential,[3] traditional hardware-based artificial neural network (ANN) designs use a weighted sum operation which is implemented in crossbars performing a series of multiply and accumulate (MAC) operations.[4] This scheme is very efficient when the neuromorphic system is trained *ex situ* on a supercomputer and the weights are transferred to the matrices only once.[5] However, any other design where the training must be done *in situ*, SNNs are preferable as the electronic elements are only active a fraction of the time.[6] Unlike ANNs, SNNs are designed to replicate the behavior of biological neural networks more accurately by considering the temporal dynamics of neuron firing patterns. The incorporation of spiking dynamics not only enhances the computational capacity of these networks but also aligns them more closely with the inherent bioplausibility of biological neural circuits. Furthermore, the adoption of an unsupervised learning paradigm, where network training is driven by the inherent structure of the data rather than labeled examples, takes inspiration from the remarkably efficient and self-organizing nature of biological neural systems. In essence, memristor-based SNNs offer advantages in event-driven computation and temporal processing, while memristor-based ANNs leverage memristors for efficient weight storage in conventional ANN architectures.[7,8] This autonomy makes unsupervised systems harder to understand and more difficult to develop. In fact, introducing unsupervised learning

Received: September 13, 2023
Revised: November 13, 2023
Accepted: November 14, 2023
Published: December 15, 2023

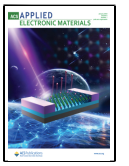

https://doi.org/10.1021/acsaelm.3c01273
ACS Appl. Electron. Mater. 2024, 6, 292−298

principles into convolutional neural networks is one of the open issues in the deep-learning community.[9]

In this work, we depart from the supervised paradigm and consider a truly unsupervised SNN which is built upon a combination of biologically plausible mechanisms similar to the one presented in the works of Diehl and Cook[10] and Querlioz *et al.*[11] It utilizes leaky-integrate-and-fire (LIF) neurons, spike-timing-dependent plasticity (STDP), lateral inhibition, and intrinsic plasticity. We particularly focus on the synapse controlled by the STDP, which is the archetypal learning rule in unsupervised systems.[12] A schematic description of the working principle of the STDP learning rule is depicted in Figure 1.

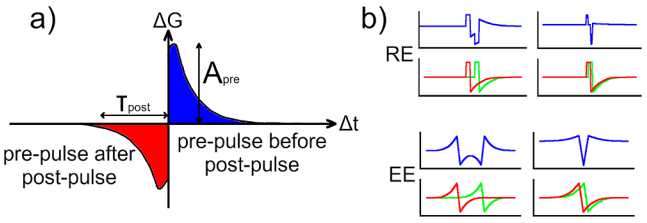

Figure 1. (a) Schematic example of a STDP measurement result. Positive Δt means that pre-pulse comes to the synapse before post-pulse, therefore increasing the conductivity. We call this blue side "pre". On the other hand, negative Δt means that pre-pulse comes after the post-pulse and the conductivity decreases. We call this red side "post". A_{pre} is the maximum relative conductance increase, and τ_{post} is the width of Δt where conductance decreases. (b) Two studied pulse shapes: RE and EE. The red and green pulses show pre- and post-pulses separately, whereas blue pulse is the combined pulse of these two. When pre- and post-pulses are close to each other, the amplitude of their combined pulse goes above the threshold voltage and therefore changes the resistance of the device.

Memristor-based SNNs hold immense potential for neuromorphic computing, yet several hurdles remain before achieving a functional prototype. SNNs employ distinct learning algorithms compared to traditional ANNs, requiring adaptation to accommodate the nonlinear and stochastic nature of memristors.[13−15] In this context, it is necessary to revisit some characteristics of the devices to make sure they are thoroughly compatible with the new learning rule paradigm (*e.g.*, we are no longer targeting control of the conductance with the accumulation of identical pulses, like most STDP works aim at MAC operations,[16−19] but a truly analog control with a single pulse). For this, we experimentally demonstrate that the fabricated synapses can be utilized in such networks and simulate the networks with the device characteristics. We have chosen to work with devices comprised of memristors of the low-bandwidth manganites $Gd_{0.3}Ca_{0.7}MnO_3$ (GCMO), which have shown promising results[20] as they exhibit good reproducibility,[21] are highly rectifying, forming-less, and compliance-free,[22] all key features for the realization of neuromorphic circuits.[23−25] The integration of these types of devices into an unsupervised SNN framework brings us closer to realizing brain-inspired computing systems with enhanced efficiency, adaptability, and bioplausibility. Through simulations, we shed light on the potential implications and applications of our findings, fostering a deeper understanding of the intricate interplay among materials, neural dynamics, and learning paradigms in the pursuit of cognitive computing.

EXPERIMENTAL SECTION

Samples. The synapses are memristor-based devices that consist of $Al/Gd_{0.3}Ca_{0.7}MnO_3/Au$ heterojunctions. We have chosen to utilize an asymmetric configuration of electrodes to ensure that only one interface is active, which creates a rectifying behavior while increasing the reliability of the devices.[20] The GCMO thin films were deposited on $5 \times 5 \times 0.5$ mm^3 (100) $SrTiO_3$ (Crystal GmbH) substrates. Deposition was done with pulsed laser deposition using XeCl laser that has a wavelength of $\lambda = 308$ nm. The pulse duration was 28 ns with repetition rate of 5 Hz. Laser fluence was 2 J/cm^2, and the pressure of the oxygen flow in the deposition chamber was 0.17 Torr. A total of 1500 pulses were used to produce approximately 70 nm thick films. Films were grown at a temperature of 700 °C with *in situ* postannealing. The Au junctions were made by making Au electrodes on the surface of the GCMO film by electron-beam physical vapor deposition (e-beam). The Al junctions were formed by bonding the Al wire directly to the surface of the GCMO with a TPT HB05 ultrasonic bonder. It is worth noting that it is not a requirement to utilize wire-bonded electrodes, as similar results were obtained in deposited Al electrodes; indicating that the functionalities explored in this work are based on intrinsic properties of the GCMO/Al interface. Furthermore, we are working on optimizations to the fabrication process to avoid utilizing wire-bonded electrodes, as they are detrimental toward scaling efforts. We have chosen to work with planar junctions instead of the more common capacitor-like structure to avoid any effect of the bottom electrode in the crystal structure of the GCMO, as it is known that a change in the crystal properties has a strong effect in the memristive response in manganite-based devices. In our particular case, we have previously reported that for thicknesses over 70 nm,[26] the bulk GCMO has a metallic-like conduction with a relative low conductivity (10^{-2} Ω·cm). Given that we also tested devices with both Au electrodes, they did not show any signs of memristive effects, and the Au/GCMO/Al device resistance is on the order of 10^6 Ω, we can assert that only a small region near the GCMO/Al contributes to the memristive effects. Details about the physical conduction mechanism and device fabrication can be found in our previous works.[20,27,28]

STDP Measurements. STDP is a biological process where neural connections are made stronger or weaker depending on the firing order of input and output signals of a neuron. If the input to the neuron, so-called pre-spike, fires just before the neurons output, post-spike, the connection is made stronger. On the other hand, if the post-spike fires before the pre-spike, then the connection becomes weaker.[29] It is the most common learning functionality utilized in unsupervised learning schemes with spike-based neural networks,[30] for which it is compulsory to have good STDP to obtain a hardware realization of such networks.

The STDP measurements were performed utilizing a dedicated memristor characterization platform, ArCOne.[31] This tool allows iteration through different sum spikes depending on the time between pre- and post-spikes Δt. It starts from $\Delta t = 0$ and continues to larger absolute values while polarity is switched every other pulse to ensure there is no drift or accumulation effect. Therefore, the largest changes to the sample's conductance happen in the beginning of the measurement. The result of the measurement is a series of $\frac{dG}{G_0}$ values as a function of Δt, where $\frac{dG}{G_0}$ is the relative change of conductance compared to the initial conductance, Δt is the time difference between the pre- and post-pulses (Figure 1). As the change in conductance upon pulsing depends on the value of conductance,[32] a great effort was taken in starting each measurement in the same value of G_0. We compared two different pulse shapes, rectangular−exponential (RE) and exponential−exponential (EE), which are schematized in Figure 1. The EE shape was chosen because it demonstrated great STDP stability in a novel insulator-to-metal transition field-effect transistor.[33] RE was selected as comparison, as it showed promising results in a study of different pulse shapes in ferroelectric memristors.[34]

https://doi.org/10.1021/acsaelm.3c01273
ACS Appl. Electron. Mater. 2024, 6, 292−298

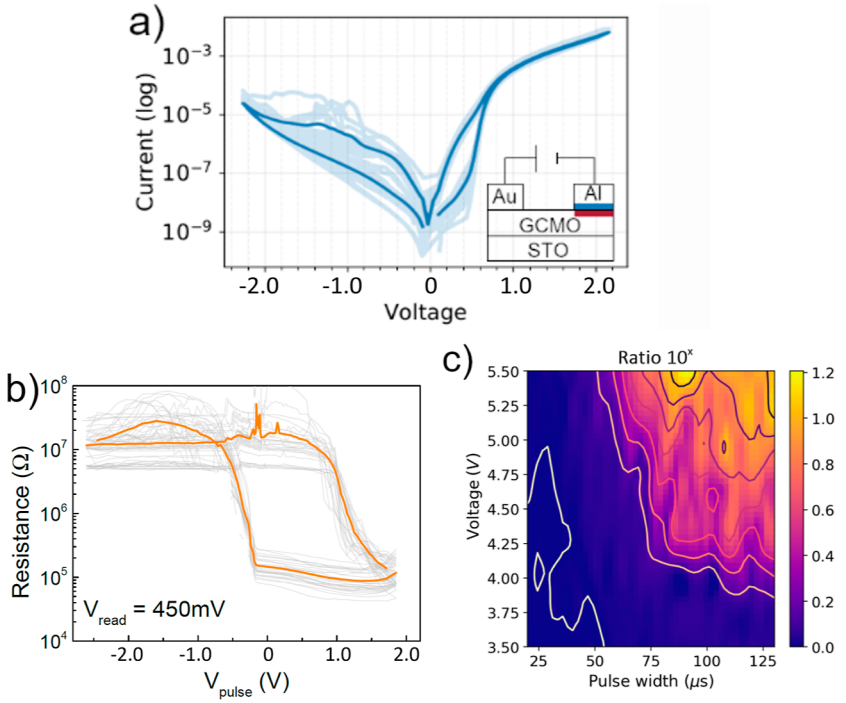

Figure 2. (a) Resistive switching in IV-loops of GCMO. We show measurements for 28 consecutive sweeps in lighter color, while the average loop is drawn in a darker color. Inset: schematic image of the device. The blue layer represents the formed AlO_x layer, and the red layer represents the oxygen-deficient GCMO. This is the active interface, where the resistive switching happens. (b) Resistive switching hysteresis loop measured for the same 28 loops as (a); the light gray curves are the raw measurements, while the orange one is the average loop. (c) Contour plot for the resistance change ratio as a function of pulse, width, and amplitude.

Spiking Neural Network Structure. To benchmark the GCMO synapses, we simulate the training and testing of multiple unsupervised SNNs to recognize handwritten digits from the MNIST database.[35] For this, we utilized a network architecture similar to other biologically plausible designs reported before,[10,11] but slightly modified to run in the newer versions of the Brian2 library.[36] Brian2 is a simulator for biological SNNs, which does not have any learning incorporated. Therefore, for the proper utilization, it is necessary to include the neuron interconnections and learning rules. We selected this setting over the more commonly employed one in machine learning to underscore the robustness of the outcomes and their biological plausibility. This approach paves the way for the development of innovative network architectures, allowing the creation of biohybrid systems in which electronic devices can potentially assist in restoring connectivity deficits in biological neurons.

RESULTS AND DISCUSSION

Device Characteristics. A schematic representation of the devices is presented in the inset of Figure 2a. Devices were designed with an asymmetric choice of electrodes. This electrode asymmetry creates a high rectification property, which grants them the capability to perform as rectifiers and voltage-controlled switches, making them indispensable in radiofrequency applications and beyond. As we contemplate the prospects of upscaling memristor technology, the presence of resistance in both low and high states becomes a key factor, as it offers opportunities to design more robust and versatile circuits by lowering the sneak path currents and acting as selector devices. In this configuration, we have one inert electrode which forms an ohmic junction, the GCMO (Au), and an active one (Al), where a small layer of AlO_x (in blue) and oxygen-deficient GCMO (in red) are formed due to the difference in work functions between the materials. This intermediate oxide layer formation has been reported in other Manganite-based devices and even introduced on purpose to stabilize the memristive effect.[37−39] The difference in the work function induces charge migration and oxygen vacancies within the GCMO, creating a localized region with altered electronic properties. This oxygen-deficient GCMO region, marked in red, becomes the dynamic core of the memristor. The switching mechanism in this configuration can be attributed to the drift and diffusion of oxygen vacancies within the active region. When an external voltage is applied across the memristor, it induces the migration of oxygen vacancies, causing a reversible change in the resistance state. This migration of oxygen vacancies results in the alteration of the local conductive path, thereby switching the memristor between its high and low resistance states.

The presence of the AlO_x layer further modulates the resistance switching mechanism by serving as a barrier that controls the flow of oxygen vacancies, thus influencing the switching dynamics. This engineered heterostructure design, with its active and inert components, enables precise control over the memristive behavior and represents a promising avenue for achieving single pulse switching events, which are necessary if STDP is to be implemented in SNNs.

To characterize the devices, we performed systematic measurements and characterized the “dynamical” and “remnant” resistive states (seen in Figure 2a,b, respectively) to gain insights into the hysteresis phenomena and design appropriate pulsing protocols to control the devices. To utilize our memristor devices as STDP synapses, it is necessary to obtain a good analog control with single pulses of varying amplitude and width. However, the first thing that is needed is a threshold behavior, where devices can be read without disturbing the memory state.

https://doi.org/10.1021/acsaelm.3c01273
ACS Appl. Electron. Mater. 2024, 6, 292−298

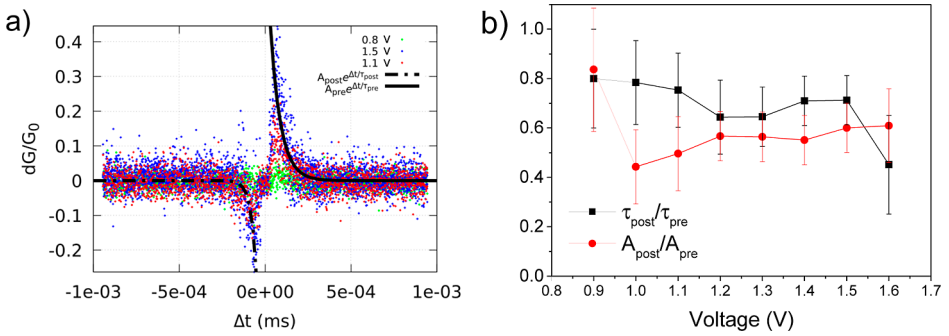

Figure 3. (a) STDP measurement curves for EE-pulsed devices with different voltage amplitudes. The shape of the STDP curve is clearly visible with a similar shape to the representative STDP curve depicted in Figure 1. However, a voltage scale of 0.8 shows no synaptic behavior as the pulses do not reach the threshold. (b) Ratio between A_{pre} and A_{post} as well as τ_{post} and τ_{pre} parameters from the EE-pulsed devices.

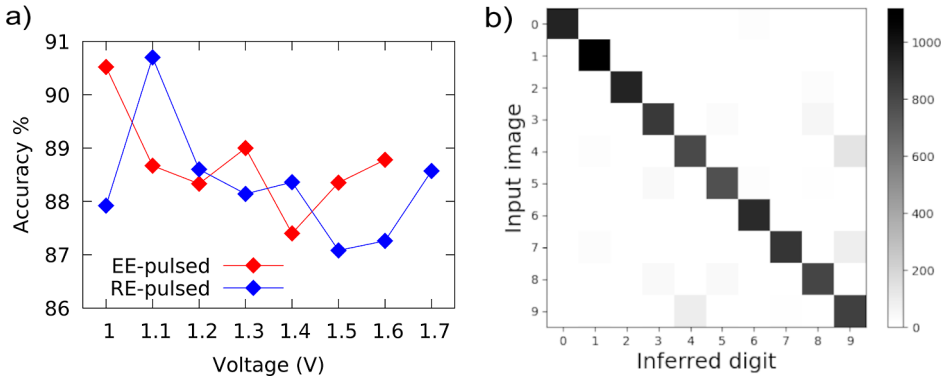

Figure 4. (a) Accuracy percentage of all the trained SNNs for both pulse protocols with respect to the voltage scale parameter. Red symbols are the ones where the synapses were pulsed with EE pulses and the blue symbols represent the RE-pulsed systems. (b) Confusion matrix of a SNN, whose synapses were based on a device pulsed with EE pulses at a voltage scale of 1.1. Rows are the inputted digits and columns are the digits the network inferred. Darker shade means it has been the output more often. For example, the digit "1" has been the most often correctly recognized digit, whereas the digit "4" tends to be mixed with the digit "9".

The threshold behavior is an important requirement that it is often overlooked and can influence the accuracy of the system over long periods of time. To probe the behavior of our devices, we performed resistive switching hysteresis loop, where we measured the remnant state with a read voltage of 450 mV after the application of a single writing pulse in a looped fashion ($0 \rightarrow V_{max} \rightarrow V_{min} \rightarrow 0$), with logarithmic amplitude progression and a pulse duration of 100 ms. The results are presented in Figure 2b. As designed, the devices have a bipolar behavior with highly asymmetric threshold voltages: (-0.12 ± 0.02) V and (0.45 ± 0.05) V for the set and reset processes, respectively. The resistance values obtained for the high and low resistance states can be tuned with great flexibility depending on the pulsing protocol.[28] This allows us good analog control of conducting states without many device-to-device or cycle-to-cycle variations.

Since the STDP will depend on the timings as well as amplitude, we performed a response map of the devices in programming pulse width and voltage amplitude (results shown in Figure 2c). The control of the conductance states was repeatable, and both high and low states can be controlled individually or both of them simultaneously. These results were used to construct the functional pulsing shape forms that STDP is based upon.

Synaptic Behavior. All the results of the STDP experiments are summarized in Figure 3a, where the relative change of the conductance is plotted as a function of the time difference between the pre-spike and post-spike pulses Δt. The GCMO-based devices show clear synaptic behavior in the voltage scale range of 0.9−1.6 V for EE pulse and 1.0−1.7 V for RE pulse. The STDP curve shapes in our results are very similar to the ones measured from the rat hippocampus and reported by Bi and Poo,[40] which further supports the biocompatibility of the synaptic capabilities of our devices. Three examples of measurement results with different applied voltages are presented; for lower voltages, there is no conductance change, as expected. The measurement data of the amplitudes that showed a change in the conductance was fitted using a two part function

$$W(\Delta t) = \begin{cases} A_{pre} e^{-\Delta t/\tau_{pre}} & \text{if } \Delta t > 0 \\ A_{post} e^{\Delta t/\tau_{post}} & \text{if } \Delta t < 0 \end{cases} \quad (1)$$

where $W = \frac{dG}{G_0}$ is the synaptic weight used in the simulated SNN, A_{pre} and A_{post} are the maximal relative change in conductance for the pre- and post-sides, Δt is the time between pre-spike and post-spike pulses, and τ_{pre} and τ_{post} are the widths of the STDP spikes for both sides. We have chosen W to quantify the synaptic weight change instead of the conductance so that our SNN code is compatible with Diehl and Cook, although for fully hardware-based applications, utilizing the conductance will be a preferable choice for the synaptic weight. An example of the fit is also included in Figure 3a for a voltage amplitude of V = 1.5 V. We found that the ratio of A_{post} and A_{pre} showed a conductance change with a small negative slope

https://doi.org/10.1021/acsaelm.3c01273
ACS Appl. Electron. Mater. 2024, 6, 292−298

with respect to applied voltage, meaning that the system responds more asymmetrically with larger input voltages. On the other hand, the ratio between τ_{post} and τ_{pre} remained constant for all voltages that showed a conductance change.

Optimization of Synaptic Properties. In both pulsing protocols, there is a rough relation between V_{pulse} and the absolute values of A_{pre} and A_{post}. This is expected, as larger voltage spikes should change the resistance of the device more dramatically. Similar to what was observed in biological synapses,[40] our devices present an asymmetry between pre- and post-conditions. In Figure 3b, we show the ratio between A_{post} and A_{pre} as well as τ_{post} and τ_{pre}. The devices present a ratio of A_{post} and A_{pre} for both EE and RE pulsing protocols with parameters close to 0.5, which according to the simulations is a requirement for good accuracy in digit recognition. On the other hand, both pulsing protocols show a ratio between τ_{post} and τ_{pre} closer to 0.75, which is constant for all applied voltages.

From the accuracy results of the simulations, we found that both the voltage scale and the ratio A_{post}/A_{pre} are related to the resulting accuracy, while τ_{post} and τ_{pre} are not. While τ are related with the pulsed width, it is worth mentioning that the actual pulsed width on the STDP measurements depends on the value of Δt and thus is not constant while obtaining the curve in Figure 3a. Given the relationship between pulse width and amplitude (Figure 2c), it is to be expected that the effect of τ will be negligible compared to the amplitude.

When looking at Figures 4a and 3b, it can be seen that both pulsing protocols show that devices that have larger ratio tend to have more accurate results. It seems like the network benefits from synapses that are more sensitive to weakening the connections rather than strengthening them. All of the accuracy results of the simulated neural networks are represented with respect to the applied voltage for both pulse shapes in Figure 4a. The best accuracies were achieved with a voltage amplitude of 1.0 for EE-pulsed synapses. The network trained with these synapses reached an accuracy of 90.52%. For RE-pulsed synapses, the best accuracy of 90.71% was reached with V_{pulse} = 1.1. There is no clear relation between V_{scale} and the accuracy of the network. However, with both pulses, the best result was achieved with relatively low pulse voltages. This is an encouraging result as it is better to use as low voltages as possible to make the devices last longer and use less energy. An example of how well a single network recognizes handwritten digits is shown as a confusion matrix in Figure 4b. In this matrix, we can see that the network predicts the digits quite well. The small number of incorrect classifications arises from mixing digits 3 and 8 with each other and also 4 and 9, which have similar shapes.

Even though the best accuracy was reached with the RE-shaped pulse, we incline to believe that the EE pulse is an optimal pulse shape. This is because the EE pulse was only 45% of the width of the RE pulse, which means that the EE pulse uses less energy than the RE pulse. This would be the case even if the width would be identical as shown in.[34] The results for EE-pulsed synapses are very similar to the ones of RE-pulsed synapses, so the energy difference will be the deciding factor. The differences between the best results of RE-pulsed and EE-pulsed synapses are minimal, and the overall results are similar to each other.

CONCLUSIONS

We investigated the synaptic characteristics of GCMO-based memristors with asymmetric electrodes. By choosing the appropriate pulse shapes, voltages, and timings, we have demonstrated that we can control the conductance of the devices in an analog matter with a single driving pulse. We utilized this information to create a pulsing scheme that allows us to utilize these devices as artificial synapses in simulated biologically plausible unsupervised neural networks. We found the optimal voltage scale and demonstrated the desired functionality for two different pulse shapes: RE and EE pulsing protocols. The simulation results show that the GCMO-based synapses work really well, and with further developments in the fabrication process toward scaling and Si integration, these devices could pave the way for real-world memristor-based SNN circuits.

It has been envisioned that unsupervised learning is necessary for the proper high-level performance of neuromorphic systems, and our artificial STDP synapse can contribute to unsupervised learning with lower energy consumption. Therefore, we believe that our GCMO-based synapse is a promising innovation for the present neuromorphic research.

AUTHOR INFORMATION

Corresponding Author

Alejandro Schulman − *Wihuri Physical Laboratory, Department of Physics and Astronomy, University of Turku, FI-20014 Turku, Finland;* Present Address: International Iberian Nanotechnology Laboratory (INL), Braga 4715-330, Portugal; orcid.org/0000-0002-8053-2626; Email: alejandro.schulman@utu.fi

Authors

Teemu Hynnä − *Wihuri Physical Laboratory, Department of Physics and Astronomy, University of Turku, FI-20014 Turku, Finland*

Ville Lähteenlahti − *Wihuri Physical Laboratory, Department of Physics and Astronomy, University of Turku, FI-20014 Turku, Finland*

Hannu Huhtinen − *Wihuri Physical Laboratory, Department of Physics and Astronomy, University of Turku, FI-20014 Turku, Finland*

Petriina Paturi − *Wihuri Physical Laboratory, Department of Physics and Astronomy, University of Turku, FI-20014 Turku, Finland*

Complete contact information is available at: https://pubs.acs.org/10.1021/acsaelm.3c01273

Notes

The authors declare no competing financial interest.

ACKNOWLEDGMENTS

The authors acknowledge the Jenny and Antti Wihuri Foundation for financial support. V. L. also acknowledges support from the University of Turku Graduate School (UTUGS).This study was supported by the Academy of Finland project 308285 as well as the Business Finland OCEAN project 344/31/2021.

https://doi.org/10.1021/acsaelm.3c01273
ACS Appl. Electron. Mater. 2024, 6, 292−298

REFERENCES

(1) Bullmore, E.; Sporns, O. The Economy of Brain Network Organization. *Nat. Rev. Neurosci.* **2012**, *13* (5), 336−349.
(2) Kim, S. G.; Han, J. S.; Kim, H.; Kim, S. Y.; Jang, H. W. Recent Advances in Memristive Materials for Artificial Synapses. *Adv. Mater. Technol.* **2018**, *3*, 1800457.
(3) Averbeck, B. B.; Latham, P. E.; Pouget, A. Neural correlations, population coding and computation. *Nat. Rev. Neurosci.* **2006**, *7*, 358−366.
(4) Hu, M.; Graves, C. E.; Li, C.; Li, Y.; Ge, N.; Montgomery, E.; Davila, N.; Jiang, H.; Williams, R. S.; Yang, J. J.; Xia, Q.; Strachan, J. P. Memristor?based analog computation and neural network classification with a dot product engine. *Adv. Mater.* **2018**, *30*, 1705914.
(5) Prezioso, M.; Merrikh-Bayat, F.; Hoskins, B. D.; Adam, G. C.; Likharev, K. K.; Strukov, D. B. Training and operation of an integrated neuromorphic network based on metal-oxide memristors. *Nature* **2015**, *521*, 61−64.
(6) Maass, W. Energy-efficient neural network chips approach human recognition capabilities. *Proc. Natl. Acad. Sci. U.S.A.* **2016**, *113*, 11387−11389.
(7) Cui, B.; Fan, Z.; Li, W.; Chen, Y.; Dong, S.; Tan, Z.; Cheng, S.; Tian, B.; Tao, R.; Tian, G.; et al. Ferroelectric photosensor network: an advanced hardware solution to real-time machine vision. *Nat. Commun.* **2022**, *13*, 1707.
(8) Chen, Z.; Li, W.; Fan, Z.; Dong, S.; Chen, Y.; Qin, M.; Zeng, M.; Lu, X.; Zhou, G.; Gao, X.; Liu, J.-M. All-ferroelectric implementation of reservoir computing. *Nat. Commun.* **2023**, *14*, 3585.
(9) Lee, C.; Panda, P.; Srinivasan, G.; Roy, K. Training deep spiking convolutional Neural Networks with STDP-based unsupervised pre-training followed by supervised fine-tuning. *Front. Neurosci.* **2018**, *12*, 435.
(10) Diehl, P. U.; Cook, M. Unsupervised learning of digit recognition using spike-timing-dependent plasticity. *Front. Comput. Neurosci.* **2015**, *9*, 1−9.
(11) Querlioz, D.; Bichler, O.; Dollfus, P.; Gamrat, C. Immunity to device variations in a spiking neural network with memristive nanodevices. *IEEE Trans. Nanotechnol.* **2013**, *12*, 288−295.
(12) Abbott, L. F.; Nelson, S. B. Synaptic plasticity: taming the beast. *Nat. Neurosci.* **2000**, *3* (S11), 1178−1183.
(13) Midya, R.; Wang, Z.; Asapu, S.; Joshi, S.; Li, Y.; Zhuo, Y.; Song, W.; Jiang, H.; Upadhay, N.; Rao, M.; Lin, P.; Li, C.; Xia, Q.; Yang, J. J. Artificial neural network (ANN) to spiking neural network (SNN) converters based on diffusive memristors. *Adv. Electron. Mater.* **2019**, *5*, 1900060.
(14) Ye, L.; Gao, Z.; Fu, J.; Ren, W.; Yang, C.; Wen, J.; Wan, X.; Ren, Q.; Gu, S.; Liu, X.; Lian, X.; Wang, L. Overview of memristor-based neural network design and applications. *Front. Phys.* **2022**, *10*, 839243.
(15) Balaji, V. N.; Srinivas, P. B.; Singh, M. K. Neuromorphic advancements architecture design and its implementations technique. *Mater. Today* **2022**, *51*, 850−853.
(16) Hu, M.; Strachan, J. W.; Merced-Grafals, E.; ZhiyongLi, H.; Williams, S. Dot-Product Engine: Programming Memristor Crossbar Arrays for Efficient Vector-Matrix Multiplication *ICCAD Workshop on "Towards Efficient Computing in the Dark Silicon Era"At*; ICCAD: Austin, 2015.
(17) Leng, K.; Yu, X.; Ma, Z.; Li, W.; Xu, J.; Xu, L.; Chen, K. Artificial synapse arrays based on SiOx/TiOx memristive crossbar with high uniformity for neuromorphic computing. *Appl. Phys. Lett.* **2022**, *120*, 043101.
(18) Choi, S.; Kim, Y.; Van Nguyen, T.; Jeong, W. H.; Min, K.-S.; Choi, B. J. Low?power self?rectifying memristive artificial neural network for near internet?of?things sensor computing. *Adv. Electron. Mater.* **2021**, *7*, 2100050.
(19) Xia, Q.; Yang, J. J. Memristive crossbar arrays for brain-inspired computing. *Nat. Mater.* **2019**, *18*, 309−323.
(20) Lähteenlahti, V.; Schulman, A.; Beiranvand, A.; Huhtinen, H.; Paturi, P. Electron Doping Effect in the Resistive Switching Properties of Al/$Gd_{1-<i>x</i>}Ca_{<i>x</i>}MnO_3$/Au Memristor Devices. *ACS Appl. Mater. Interfaces* **2021**, *13*, 18365−18371.
(21) Hu, M.; Strachan, J. P.; Li, Z.; Grafals, E. M.; Davila, N.; Graves, C.; Lam, S.; Ge, N.; Yang, J. J.; Williams, R. S. Dot-product engine for neuromorphic computing. *Proceedings of the 53rd Annual Design Automation Conference*; ACM: New York, NY, USA, 2016.
(22) Jang, J. W.; Park, S.; Burr, G. W.; Hwang, H.; Jeong, Y. H. Optimization of Conductance Change in $Pr_{1-<i>x</i>}Ca_{<i>x</i>}MnO_3$-Based Synaptic Devices for Neuromorphic Systems. *IEEE Electron Device Lett.* **2015**, *36*, 457−459.
(23) Ielmini, D. Brain-inspired computing with resistive switching memory (RRAM): Devices, synapses and neural networks. *Microelectron. Eng.* **2018**, *190*, 44−53.
(24) Kim, T.; Hu, S.; Kim, J.; Kwak, J. Y.; Park, J.; Lee, S.; Kim, I.; Park, J. K.; Jeong, Y. J. Spiking Neural Network (SNN) With Memristor Synapses Having Non-linear Weight Update. *Front. Comput. Neurosci.* **2021**, *15*, 646125.
(25) Zhao, M.; Gao, B.; Tang, J.; Qian, H.; Wu, H. Reliability of analog resistive switching memory for neuromorphic computing. *Applied Physics Reviews* **2020**, *7*, 011301.
(26) Schulman, A.; Beiranvand, A.; Lähteenlahti, V.; Huhtinen, H.; Paturi, P. Appearance of glassy ferromagnetic behavior in Gd1-xCaxMnO3 ($0 \leq x \leq 1$) thin films: A revised phase diagram. *J. Magn. Magn. Mater.* **2020**, *498*, 166149.
(27) Lähteenlahti, V.; Schulman, A.; Huhtinen, H.; Paturi, P. Transport properties of resistive switching in Ag/Pr0.6Ca0.4MnO3/Al thin film structures. *J. Alloys Compd.* **2019**, *786*, 84−90.
(28) Miranda, E.; Lahteenlahti, V.; Huhtinen, H.; Schulman, A.; Paturi, P. Compact modeling and SPICE simulation of GCMO-based resistive switching devices. *IEEE Trans. Nanotechnol.* **2022**, *21*, 285−288.
(29) Buonomano, D. V.; Carvalho, T. P. *Encyclopedia of Neuroscience*; Elsevier Ltd, 2009, pp 265−268.
(30) Pedroni, B. U.; Joshi, S.; Deiss, S. R.; Sheik, S.; Detorakis, G.; Paul, S.; Augustine, C.; Neftci, E. O.; Cauwenberghs, G. Memory-Efficient Synaptic Connectivity for Spike-Timing- Dependent Plasticity. *Front. Neurosci.* **2019**, *13*, 357.
(31) Arc Instruments. *Memristor Characterisation Platform User Manual*, 2017.
(32) Stoliar, P.; Levy, P.; Sanchez, M. J.; Leyva, A. G.; Albornoz, C. A.; Gomez-Marlasca, F.; Zanini, A.; Toro Salazar, C.; Ghenzi, N.; Rozenberg, M. J. Nonvolatile multilevel resistive switching memory cell: A transition metal oxide-based circuit. *IEEE Trans. Circuits Syst. II Express Briefs* **2014**, *61*, 21−25.
(33) Stoliar, P.; Schulman, A.; Kitoh, A.; Sawa, A.; Inoue, I. H. STDP synapse with outstanding stability based on a novel insulator-to-metal transition FET *2017 IEEE International Electron Devices Meeting (IEDM)*; IEEE, 2017;.
(34) Stoliar, P.; Yamada, H.; Toyosaki, Y.; Sawa, A. Spike-shape dependence of the spike-timing dependent synaptic plasticity in ferroelectric-tunnel-junction synapses. *Sci. Rep.* **2019**, *9*, 17740.
(35) Deng, L. The MNIST Database of Handwritten Digit Images for Machine Learning Research [Best of the Web]. *IEEE Signal Process. Mag.* **2012**, *29*, 141−142.
(36) Stimberg, M.; Brette, R.; Goodman, D. F. Brian 2, an intuitive and efficient neural simulator. *eLife* **2019**, *8*, No. e47314.
(37) Herpers, A.; Lenser, C.; Park, C.; Offi, F.; Borgatti, F.; Panaccione, G.; Menzel, S.; Waser, R.; Dittmann, R. Spectroscopic proof of the correlation between redox-state and charge-carrier transport at the interface of resistively switching Ti/PCMO devices. *Adv. Mater.* **2014**, *26*, 2730−2735.
(38) Kanegami, N.; Nishi, Y.; Kimoto, T. Unique resistive switching phenomena exhibiting both filament-type and interface-type switching in Ti/$Pr_{0.7}Ca_{0.3}MnO_{3-\delta}$/Pt ReRAM cells. *Appl. Phys. Lett.* **2020**, *116*, 013501.
(39) Yang, R.; Li, X. M.; Yu, W. D.; Liu, X. J.; Cao, X.; Wang, Q.; Chen, L. D. Multiform resistance switching effects in the Al/$La_{0.7}Ca_{0.3}MnO_3$/Pt structure. *Electrochem. Solid State Lett.* **2009**, *12*, H281.

https://doi.org/10.1021/acsaelm.3c01273
ACS Appl. Electron. Mater. 2024, 6, 292−298

(40) Bi, G. Q.; Poo, M. M. Synaptic modifications in cultured hippocampal neurons: Dependence on spike timing, synaptic strength, and postsynaptic cell type. *J. Neurosci.* **1998**, *18*, 10464−10472.

https://doi.org/10.1021/acsaelm.3c01273
ACS Appl. Electron. Mater. 2024, 6, 292−298